JMEPEG (2023) 32:6850–6865
https://doi.org/10.1007/s11665-022-07579-6

1059-9495/$19.00

TECHNICAL ARTICLE

Prediction of Mechanical Properties of Sensitized Stainless Steel by Neural Network Modeling and Validation Using Ball Indentation Test

Mousumi Das, G. Das, and M. Ghosh

Submitted: 9 June 2022 / Revised: 21 September 2022 / Accepted: 14 October 2022 / Published online: 3 November 2022

Elevated temperature sensitization of a 304 stainless steel results in degradation of mechanical properties and becomes prone to premature failure. In the present investigation, sensitization of 304 stainless steel has been done in the temperature range of 500–800 °C. Yield strength, ultimate tensile strength and fracture toughness (K_{Jc}) of the sensitized 304 stainless steel specimens were determined by ball indentation technique. Microstructural characteristics were quantified and used in artificial neural network to predict the mechanical properties of the investigated alloy. Neural network was developed with the help of MATLAB toolbox. Best equation was fitted for training, testing and validating the output. Predicted values from the developed model exhibited impressive correlation with experimental data obtained through ball indentation technique as well as with literature reports. The model has proved its distinctive potential in predicting the mechanical properties of sensitized 304 stainless steel, which faces restriction in bulk sampling from original component to perform conventional mechanical test during service exposure.

Keywords heat treatment, mechanical testing, metallography, modeling and simulation, stainless steel

1. Introduction

304 stainless steels (304SS) are widely used in nuclear industry as storage of uranium oxide balls, pressure tube, containment vessel, heat exchanger and cladding material due to their excellent resistance to corrosion, adequate elevated temperature strength and outstanding room temperature mechanical properties (Ref 1-4). During service, depending on the nature of the reactor, the alloy experiences degradation of properties in the temperature range of either 500-800 °C (high temperature short duration) or 350-475 °C (low temperature long duration) (Ref 5). Apart from the influence of temperature, the degeneration of the alloy is steered by irradiation within nuclear reactor. Disintegration of austenitic stainless steel in nuclear reactor includes phase transformation like occurrence of σ phase, phase separation like partitioning of Cr and Fe to form Cr-rich and Fe-rich phases, carbide precipitation and change in nature of defects along with density. Out of these changes, irradiation dose dominantly affects the corrosion resistance, dimensional stability and mechanical properties of 304SS. Microstructural change of the alloy at elevated temperature related to deterioration in corrosion resistance property is commonly termed as 'sensitization.' Sensitization refers to Cr-rich carbide precipitation along the austenitic grain boundary. The phenomenon makes the alloy susceptible to inter-granular corrosion and stress corrosion cracking (Ref 6). Sensitization significantly reduces the tensile strength and impact property of the alloy (Ref 7).

Sensitization and its effect on component life cycle are well documented over the years (Ref 8). Considering stringent service condition, sensitization becomes unavoidable for certain applications. The severity of sensitization gradually increases depending on temperature and duration of exposure. Therefore, it is essential to assess the effect of sensitization on the residual life of the component during service. Conventional mechanical tests need extraction of representative specimens of sufficient volume from components under critical application in nuclear power plant. Thus, sampling in turn destroys expensive module and propels mandatory shut down of the plant.

Necessity thus arises to evaluate material properties intermittently to predict the extent of degradation, explore the scope of rejuvenation and assess the residual life for safe utilization without carrying out conventional full-length test. A reliable technique, complimentary to conventional destructive tests, has a great impetus in this respect. The technique should be capable in quantifying the then state of the component in reasonable time scale without affecting the operational schedule of the system. In this respect, in situ nondestructive methods and different minimally invasive procedures like ball indentation technique (BIT), impression creep (IC), shear punch experiment (SPE) and small punch creep (SPC) have come in limelight (Ref 9). Among all these, BIT has emerged as one of the potent reliable approaches to determine mechanical properties of materials (Ref 10-16).

The method is versatile in nature considering its approach and applicability for various materials. During BIT, deformation and stress beneath the ball are multiaxial. To explore it in detail, Samal and his colleagues proposed hybrid algorithm to estimate equivalent stress and plastic strain at highly stressed

Mousumi Das, G. Das, and **M. Ghosh**, Materials Engineering Division, CSIR-National Metallurgical Laboratory, Jamshedpur 831007, India. Contact e-mail: ghosh_mnk@yahoo.com.

location below the surface of ball (Ref 17). It was assumed, that stress and strain were governed by applied load, yield stress of material and strain hardening exponent. The proposed approach was found suitable for drawing equivalent stress–plastic strain plot for wide range of materials. Selected mechanical properties of deformed 316L stainless steel was determined using BIT by Xue and his co-workers (Ref 18). Impressive correlation has been reported between mechanical properties and nature of indentation. The outcome was validated using finite element technique. Nanocomposites consisting of Mg alloy matrix reinforced with ZrO_2 and TiO_2 were also investigated using BIT (Ref 19). An instrumented indentation test was attempted for Al alloy and stainless steel by a different group of researchers (Ref 20). Equivalent elastic modulus and hardness were predicted from the experiment. Using finite element simulation and geometry of indentation, a constitutive model of plasticity was developed for both alloys. In a new approach, additive manufacturing (AM) was clubbed with instrumented spherical ball indentation technique (Ref 21). Using AM technique Ti-xNb functionally graded material was produced. Bulk hardness, Young's modulus, yield stress and work-hardening coefficient were evaluated by BIT for the fabricated component. The results of BIT were compared with conventional mechanical tests and exhibited reliability. It has been concluded that component produced with different AM parameters can be investigated using BIT without carrying out full length mechanical tests. BIT was also applied for determining yield strength and residual stress at different zones of welded assembly consisting of HY-80 and HY-100 steels (Ref 22). Comparing with conventional test, yield strength of miniature specimens exhibited a variation of $\leq$ 10%. Residual stress determined through BIT revealed consistent relation with the outcome of x-ray diffraction study. The method has been further applied for evaluating local mechanical properties of welded assembly consisting of P92 steel (Ref 23). It is also noteworthy that even for a highly heterogeneous structure containing transition joint between low-alloy steel and stainless steel, the technique has been found useful during evaluation of mechanical properties of different zones across weld centerline (Ref 24).

Apart from BIT, which involves experimentation, another feasible solution to combat with the issue of structural degradation of stainless steel, is the development of robust mathematical model. The model may able to predict the mechanical properties of the alloy accurately after pre-defined service exposure. Artificial neural network (ANN) has been originated as a research field of artificial intelligence (AI) and is a promising modeling application. ANN is useful in such situation, where existing mathematical models become inadequate / incompetent to deliver statistically reliable and reproducible outcome. In this model, selective inputs are given to obtain an output. Inputs are measured parameters, acquired during experimentation. The methodology was inspired from the biological behavior of the set of neurons and the structure of the brain (Ref 25, 26). In multilayered ANN model, there are three type of layers, which are organized hierarchically (Ref 27). The first layer is input, which receives information from the set of experimental data. The second layer is the hidden layer, which is located between input and output of the algorithm. Finally, the last layer is output, resemblances with neurons to perform the necessary processing. The basic approach of ANN model involves 'creation' and 'training.' Creation is the development of skeleton, which can operate at a given logic. Training refers to establishing consistent relation between input and output using 'neurons' by trials. Once the model has been trained to the desired level, ANN becomes capable in evaluating outputs from new process inputs. Considering the versatility of the approach, attempts have been made to apply the technique in different domains of material science (Ref 28-34). The application of ANN for predicting the degradation of 304SS, exposed in sensitization environment, is scanty in the open domain literature.

As mentioned earlier, there is always an embargo in real-time full-length tests of critical components made of 304 stainless steel in nuclear power plants. However, for safety and un-interrupted operation, it becomes essential to measure the degree of structural degeneration. Real-time evaluation of post-irradiated structurally degraded specimen needs neutralization treatment before experimentation to avoid health hazards. This may include storage in 'cooling pool' for prolong period, application of 'hot cells' and transmutation. Therefore, in the present context, it was not possible to replicate the exact physical condition that a material may experience within nuclear reactor; however, the thermal condition has been selected carefully so that the elevated temperature range may be close to the thermal condition of 304SS within reactor. The temperature ranges thus corresponded to the specified sensitization temperature of the alloy.

In the proposed investigation, the microstructural information of sensitized 304 stainless steel was utilized to develop an ANN-based model for determining the mechanical properties of the alloy. Experimental validation of data for same specimens was done by Ball Indentation Technique (BIT). Both outcomes were compared to explore reliability. Thus, the combination of ANN with BIT opens up a new domain of material evaluation efficaciously and establishes authenticity to replace conventional destructive characterization.

2. Experimental Details

2.1 Material

304SS was received in rolled condition having thickness $\sim$ 10 mm. Bulk chemical composition of base material in wt.pct was 0.07 C, 18 Cr, 8 Ni, 0.75 Si, 0.045 P and 2.0 Mn.

2.2 Heat Treatment

Detail of the sensitization treatment is listed in Table 1. As-received sample was sectioned, solutionized at $\sim$ 1080 °C for 20 h. 304 stainless steel consists of single phase austenite; however, depending on processing and thermal history, the alloy may contain δ-ferrite, M_7 carbide, M_{23} carbide, Fe-rich carbide, σ-phase, and Cr-rich nitride. Aging without solutionization may create substantial heterogeneity when these phases become preexisting. Quantification of second phase is erroneous in such case as precipitation from single phase and in the presence of preexisting second phase in same system varies widely in number density. Achieving single phase also provided another flexibility of obtaining selective precipitation (here Cr-rich carbide) during thermal treatment, contributing in embrittlement during sensitization.

Solutionization was followed by forced air cooling, for which the cooling rate was $\sim$ 11 °C/s. This cooling rate was sufficient even at $\sim$ 5 mm depth (i.e., at center with obviously

Table 1 Schedule of heat treatment for different specimens

Sl. No	Specimen ID	Heat treatment
1	H	As-received
2	H1	Solutionized at 1080 °C for 20 h
3	H2	Solutionized at 1080 °C for 20 h and sensitized at 500 °C for 5 h
4	H3	Solutionized at 1080 °C for 20 h and sensitized at 600 °C for 5 h
5	H4	Solutionized at 1080 °C for 20 h and sensitized at 700 °C for 5 h
6	H5	Solutionized at 1080 °C for 20 h and sensitized at 800 °C for 5 h

reduced value) for the investigated specimen to retain austenitic microstructure (Ref 35). Moreover, it has been indicated in subsequent section that major precipitating phase in austenitic stainless during thermal aging was Cr-rich carbide. Substantial extent of Cr-rich carbide precipitation during sensitization treatment occurs at the cooling rate of ≤ 0.5 °C/s (Ref 36). Thus, the solution heat treatment followed by forced air cooling ensured single phase for the given dimension of austenitic stainless steel.

Solutionized specimens were further sensitized at various temperatures to facilitate microstructural changes. Sensitization temperatures have been selected based on different temperature ranges that may be encountered by the alloy during actual service exposure in nuclear reactor (Ref 37).

2.3 Characterization

Sensitized specimens were prepared using conventional metallographic technique for microstructural investigation. Specimens were etched with Glycergia (mixture of nitric acid + hydrochloric acid, with the addition of few drops of glycerine) to reveal microstructure. Prepared specimens were examined in scanning electron microscopes (SEM, Hitachi SU7000). For particular specimen, minimum five numbers of un-biased imaging have been carried out from different locations at suitable magnification. These images were used in 'Image-J' software for exploring quantitative metallographic information. During processing, the magnification bar was calibrated and grayscale thresh holding was done for different structural features. Subsequently, quantitative analysis of the same characteristics has been carried out, which included determination of matrix grain size, diameter of second phase particles and area fraction of precipitates. The same procedure was repeated for all specimens under investigation. The average value with error bar has been considered for different features in the manuscript.

2.4 Mechanical Tests

To study mechanical properties of sensitized specimens, a Portable Automated Ball Indentation (PABI) unit was used. Schematic of the PABI system is shown in Fig. 1. Working principle of BIT involves loading and unloading of a tungsten carbide ball (indenter) against the selected material, resulting an alternative compressive stress on the material (Ref 13). The diameter and hardness of the ball were 1.5 mm and > 70 HRC, respectively. Indentation depth (both elastic and total)

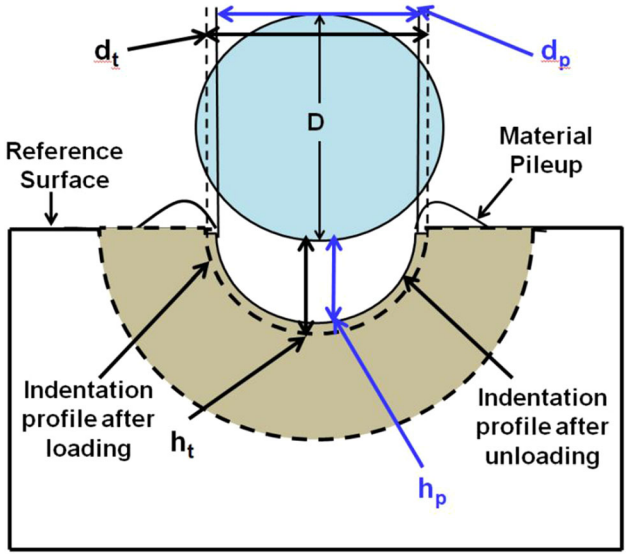

Fig. 1 Schematic of Indentation profile during loading and unloading conditions

due to compressive stress by the indenter during loading and unloading was plotted as a function of load. The uniform compressive stress over specimen surface by indenter generates a stress-controlled flow curve. Deformation height was measured by a linear variable differential transducer (LVDT), attached with PABI system. Indentation depth of each loading/unloading cycle was used for computing the diameter of the indentation. Data were further converted into true stress–strain plot to find out yield strength, ultimate tensile strength, hardness and fracture toughness of the material (Ref 10-12, 14).

In this study, deformation of all the specimens took place under load-controlled mode. For each load/unload cycle, corresponding depth (both elastic and plastic) was measured using LVDT. Tensile properties of each specimen were evaluated by considering eight loading and unloading cycles of load–depth curves. For each loading cycle total indentation depth (h_t) and corresponding total diameter (d_t) were obtained under maximum load. After completing each unloading cycle, plastic indentation depth (h_p) and related plastic indentation diameter (d_p) were recorded. The values of h_t, h_p, d_t, d_p for a given load (kN) were used as raw data for determining the mechanical properties.

Different equations used for evaluating mechanical properties of materials by PABI are tabulated in Table 2.

2.5 ANN Model

An artificial neural network is an interconnected group of nodes, inspired by a simplification of neurons in a brain. In this study, back-propagation and Levenberg–Marquardt algorithms were used. In the artificial neural-networks field, the Levenberg–Marquardt algorithm is remarkably efficient and well accepted for training small- and medium-sized problems. Back-propagation algorithm is a delta rule or gradient descent technique and one of the most well-known algorithms for training the multilayer perceptron (Fig. 2).

This approach minimizes the error for a particular training pattern by adjusting the weights. In this study, the training of algorithm by backpropagation has been utilized in one feed-forward hidden layer.

Table 2 Equations used for evaluating the mechanical properties of stainless steel

Sr. No	Parameter / Variables	Governing equation & used notations	References
1	Ultimate tensile strength (σ_{uts})	$\sigma_{uts} = (K/e)^n$ K strength coefficient, n strain hardening exponent and e constant (~ 2.71) K and n can be determined through regression analysis of power law equation for different values of $\boldsymbol{\sigma}$ (true stress) and $\varepsilon_{\mathbf{p}}$ (true plastic strain)	Ref 38
1.ii	True stress (σ) and Plastic strain (ε_p) [Corridere's criterion]	$\sigma = K.\varepsilon_p{}^n$ Value of σ and ε_p can be obtained using data points of load (P) and indentation plastic diameter (d_p)	Ref 10
1.ii	Load (P) and Indentation plastic diameter (d_p)	$\varepsilon_p = 0.2(d_p/D)$ $\sigma_t = 4.P \Big/ \pi d_p^2.\delta\prime$ D diameter of indenter, δ' is parameter related to deformation of materials	
1.iii	Indentation plastic diameter (d_p) [Regression analysis of the Hertzian equation]	$d_p = \sqrt[3]{2.735P\left(\frac{1}{E_1}+\frac{1}{E_2}\right)D\left\{\frac{h_p^2+0.25d_p^2}{h_p^2+0.25d_p^2-h_pD}\right\}}$ E_1 and E_2 are the Young's modulus of the indenter and the specimen under test, respectively h_p is plastic depth of the indentation	
1.iv	Parameter $\boldsymbol{\delta'}$	$\delta' = 1.12 + \tau ln\varphi$ φ is a function of a parameter τ; value depends on the flow stress and plastic strain of the test piece. Moreover, τ is a function of α_m, which is dependent on strain rate sensitivity and work hardening characteristic of the test material An iteration method has been applied to determine δ' value by using PABI software	
2	Yield strength (σ_y)	$\sigma_y = \beta_m$. A β_m is the material constant and irrespective of material's thermal/mechanical history. It can be calculated with a known value of σ_y A is material's yield parameter	
2.i	Applied load (P) and total indentation diameter (d_t) [Meyer relation]	$P/d_t^2 = A(d_t/D)^{m-2}$ A may be obtained from regression analysis of P/d_t^2 versus d_t/D test data, m is the Meyer's coefficient, D is the diameter of the indenting ball	Ref 28
2.ii	Total indentation diameter (d_t)	$d_t = 2\left(h_t.D - h_t^2\right)^{0.5}$ Total penetration depth (h_t) is measured during application of load from the corresponding load–deflection curve	
3	Brinell hardness number (HB)	$HB = \frac{2P}{\pi.D\left(D-\sqrt{\left(D^2-d_t^2\right)}\right)}$ P applied load, D diameter of ball, d_t diameter of indentation	

At the beginning, all input data were normalized for multilayer perceptron networks to teach the algorithms. All the variables were normalized by using Eq 1.

$$X_n = \left[\frac{(X_i - X_{\min})}{(X_{\max} - X_{\min})}\right] \quad \text{(Eq 1)}$$

where X_n was the normalized value and X_i was the experimental value to be normalized. $X_{\max}$ and $X_{\min}$ were the minimum and maximum values, respectively, for input within array.

Structure of the network was defined with activation functions, initialization of weights and biases. Definition of the parameters was associated with error goal and maximum number of epochs with the training algorithm. Accordingly, the algorithm was described and the neural network was trained. The main focus in model training was minimization of the mean square error (MSE). MSE of the experimental and the predicted data was used to find out the accuracy of the model and was defined as:

$$MSE = \frac{1}{MN}\sum_{x=1}^{M}\sum_{y=1}^{N}[T_i(x) - P_i(x)]^2 \quad \text{(Eq 2)}$$

where M and N were the number of training inputs and test samples, respectively. T was the target output and P was the predicted output by model network. Initially, the simulated output of the neural network was examined with the measured input data and subsequently, compared with the measured output. Finally, validation was performed with independent data.

A general structure of ANN model is shown in Fig. 3. Input variables were matrix grain size, % area fraction of second phase and size of second phase for different sensitized 304SS specimens (Table 3). Output is ultimate tensile strength (UTS), yield strength (YS) and fracture toughness of the investigated samples.

The range of input variables for sensitized SS304 is shown in Table 4. Accordingly, the outputs were also included in the table. The neighboring layers' neurons were interconnected by all weights. From the total input data, 80% of the same was randomly selected to train the network. Twenty percent data were used for testing and validation of the network. The predicted results were compared against experiment outcome.

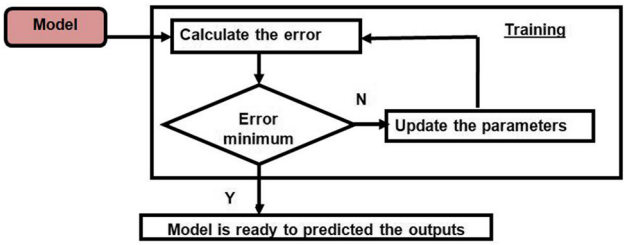

Fig. 2 Line diagram of back propagation model (BPM)

Table 3 The neural network data used in ANN model

Parameters	ANN model
Number of input layers	3
Number of hidden layers	2
Number of first hidden layers	7
Number of second hidden layers	4
Number of output layers	3

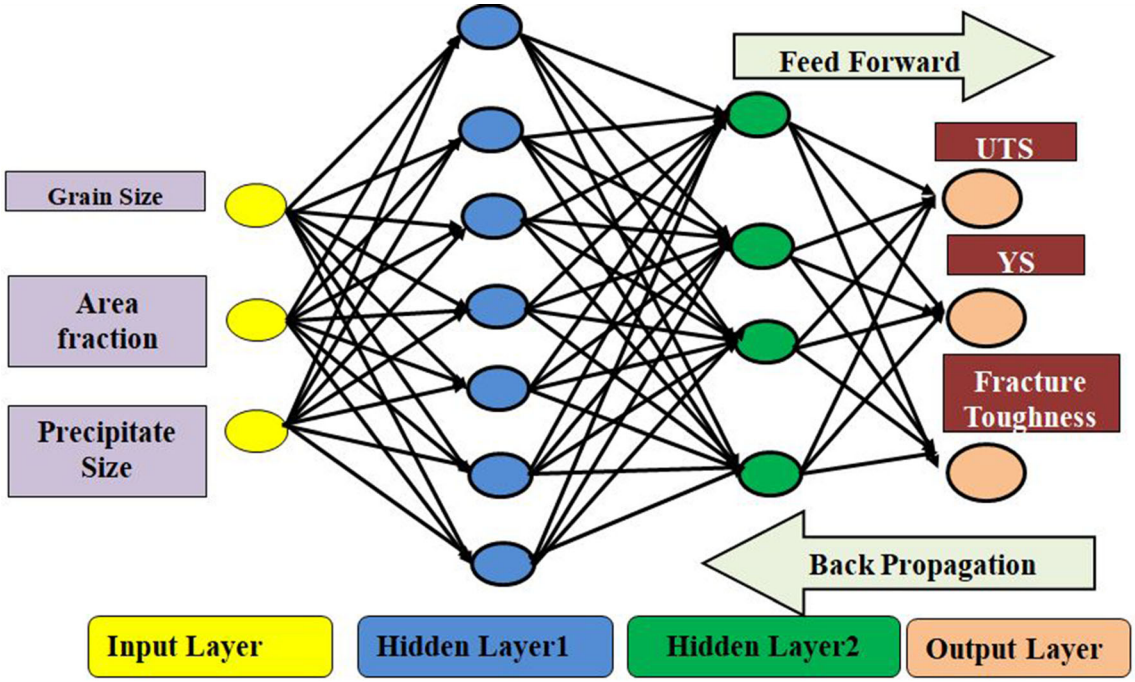

Fig. 3 The architecture of multilayer perceptron neural network (ANN) model

Table 4 Range of input and output variables used in ANN for sensitized 304SS

Sl. No	Parameters	Min	Max	Mean	Standard Deviation
Input					
1	GS(μm)	163	311	237	47.6
2	AF %	0.33	1.11	0.86	0.325
3	Prec. Size (nm)	80.5	119.6	103.26	11.7
Output					
4	UTS(MPa)	422	605.8	573.7	63.1
5	YS(MPa)	188.3	280.3	255.03	27.82
6	Fracture toughness (MPa.M$^{1/2}$)	137.94	178.02	164.14	9.5

3. Results

3.1 Tensile Properties of the Specimens

Load–deflection (P–d) curves were obtained by PABI test for one of the selected specimens. A representative P–d curve has been considered for further analysis. P–d curve of as-received stainless steel sample has been converted into true stress–true plastic strain (σ_t–ε_p) plot. The plot was compared with true stress–true strain curve, obtained through conventional tensile test (Fig. 4). It was evident that both the curves were analogous to each other without any noteworthy deviation. Therefore, BIT endorsed its reliability in evaluating mechanical properties of the alloy. Accordingly, other load–deflection (P–δ) curves were drawn using the outcomes of BIT for sensitized specimens (Fig. 5a). The plots were further converted to true stress–true strain diagram from the loading–unloading curves (Fig. 5b).

The flow stress of the alloy exhibited descending trend after solutionization treatment (Fig. 5). However, it showed sharp upward trend with the increment in sensitization temperature. The tensile properties and hardness of the specimens obtained using BIT are depicted in Table 5.

Sample H presented the alloy in rolled condition, whereas sample H1 referred to solutionized condition of the same alloy. Therefore, difference in their mechanical properties is quite evident in Table 5.

Both UTS and YS were increased steadily with the increment in sensitization temperature, reached the consummate point at $\sim$ 700 °C, and then reduced at $\sim$ 800 °C. In the same context, strain hardening exponent was decreased and the strength coefficient was enhanced monotonically with the increment in sensitization temperature. Sample H5 displayed a different characteristic in comparison to other specimens.

3.2 Microstructural Investigation

Microstructure of 304 SS under different sensitized conditions is shown in Fig. 6. By and large all specimens exhibited the presence of polygonal austenitic grains containing twins. Average matrix grain size of the specimens is furnished in Table 6. The samples were further examined in SEM. Predominantly precipitation of the sensitized samples occurred along grain boundary with few of them within grain interior (Fig. 7). Change in number density and average size distribution of second phases at various sensitized temperatures are shown in Fig. 8.

It is noteworthy that the number density of particles was increased with the enhancement in sensitization temperature, reached a maximum at $\sim$ 700 °C, and then reduced at $\sim$ 800 °C. The average particle size distribution also revealed significant variation for the sensitized specimens. The peak value of particle size shifted toward right with the increase in the temperature. The phenomenon showed that the enhancement of sensitizing temperature resulted in replacement of relatively finer particles by coarser second phases.

Figure 9(a) and (b) displays the effect of matrix grain size and area fraction of precipitates on the flow curve of different 304SS specimens. A negative correlation between indentation depth and grain size was obtained, and the same trend has been also observed for particle distribution for different specimens, except sample H5.

Strengthening mechanism of any alloy steel is the synergistic effect of solid solution hardening, dislocation hardening, transformation hardening, grain size, internal friction and precipitation hardening (Ref 39). In multicomponent system, where precipitation occurs, major contribution toward yield strength occurs due to second phase. In this respect, the contribution of grain size, solid solution strengthening and internal friction become meagre. It has been reported, that during aging of two different grades of stainless steels at 650-750 °C for various time scales promoted precipitation in austenite matrix (Ref 40). These second phases contributed significantly toward the change in mechanical properties of alloys. In welded microstructure of austenitic stainless steel, the extent of precipitation has been evaluated at different sub-zones and it was inferred that carbide precipitation became the key phenomenon to alter mechanical properties of different regions (Ref 41). The effect of structural features on crack propagation in the temperature range of − 196 to 649 °C was evaluated during fatigue testing of austenitic stainless steel (Ref 42). It was found that carbide precipitation was a dominant mechanism in controlling the deformation of the alloy. The effect of grain size and carbon variation for 300 series austenitic stainless steel was investigated using different thermal parameters. Evolution of various precipitates was discussed, and it was inferred that second phases were primarily responsible for the alteration of properties of steel (Ref 43). The effect of $M_{23}C_6$ carbide precipitation on mechanical properties of 9Cr18 austenitic stainless steel under different thermal condition was studied, and it was reported that the change in hardness was mainly contributed by carbides (Ref 44). Thus, literature reports endorse the dominant effect of second phase on the mechanical properties of thermally treated austenitic stainless steel; accord-

ingly, in the present investigation the characteristics of second phases in sensitized 304SS has been considered as primary contributor to the variation in mechanical properties of the alloy.

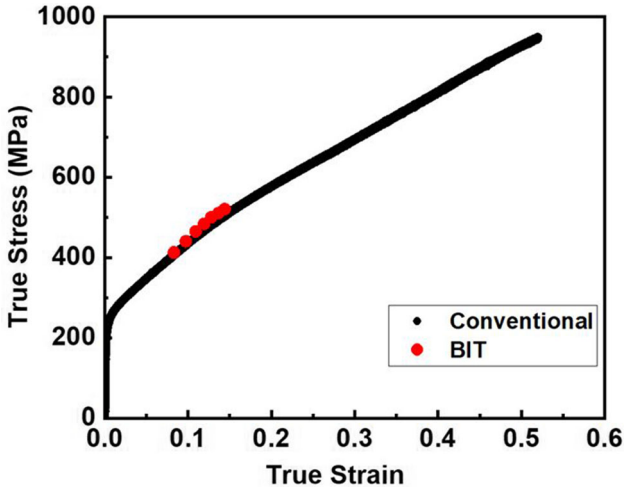

Fig. 4 Comparison of flow properties obtained from ball indentation and conventional tensile test for as received 304SS specimen

3.3 ANN Modeling with MATLAB

ANN model with Back-propagation multilayer feed forward was developed using the Neural Network Toolbox in MatlabR2019a package. As mentioned earlier, ANN model comprised of three input layers, two hidden layers and three output layers for the training (Fig. 10).

During the training process, the weight and bias values between these layers were adjusted for the experimental input and target values by altering the number of iterations, hidden nodes and layers.

Figure 11 shows the performance of the test procedure and the results obtained from the ANN model for data set, used in training, testing and validation of the model. The normalized ANN experimental outputs illustrated robust agreement with the predicted outputs. High value of R^2 of all the curves endorsed that the proposed ANN model became extremely reliable in predicting UTS, YS and fracture toughness precisely for sensitized 304 stainless steel.

Developed model was further used in evaluating mechanical properties of sensitized 304 stainless steel using microstructural information. A set of fifteen random test input data were fed into the ANN model. The model delivered numerical value of UTS, YS and fracture toughness with minor variation (Fig. 12).

The predicted values of UTS, YS and fracture toughness were compared with BIT data (Fig. 13). Five remaining BIT data set were used to validate the potential and ability of the ANN model. Table 7 shows the predicted and validation set for

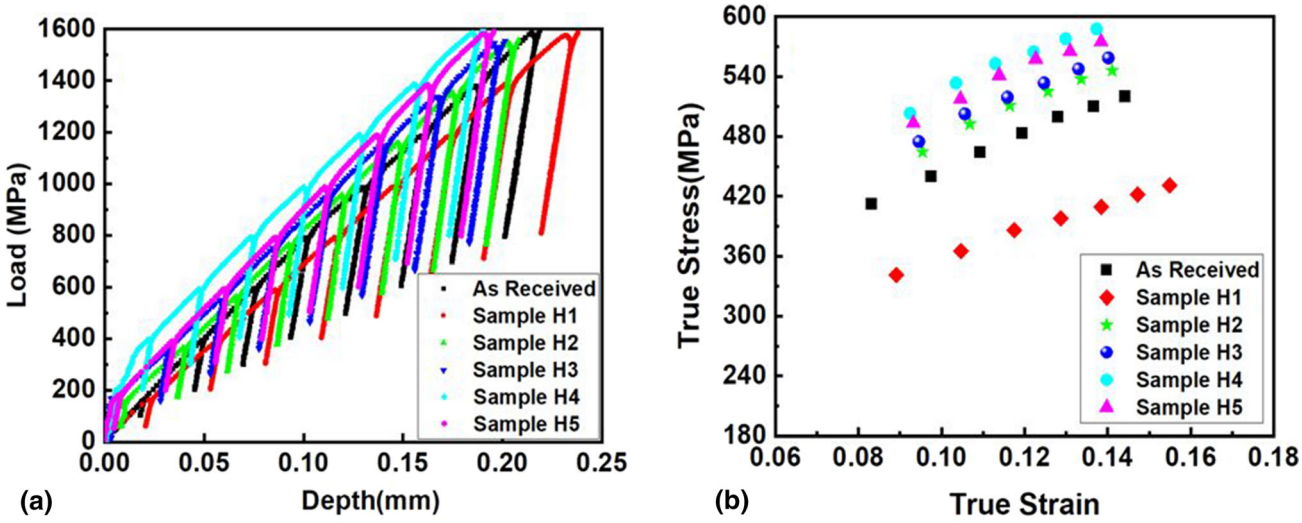

Fig. 5 Ball indentation test of various sensitized 304SS specimens (a) load–deflection curves (b) true stress–strain scatter plot

Table 5 Mechanical properties of different 304SS specimens using BIT

Sample I.D	UTS, MPa	0.2% Off set yield, MPa	Strain hardening Coeff., *n*	*K*, MPa	Hardness (HB)
H	564 ± 11 (Conv.)	224 ± 21 (Conv.)	0.40 ± 0.07 (Conv.)	1140 ± 32 (Conv.)	143 ± 5 (Conv)
	545.6 ± 15	220.4 ± 14	0.43 ± 0.1	1204.3 ± 21	141.2 ± 7
H1	430.4 ± 7	194.6 ± 11	0.42 ± 0.075	940.9 ± 13	119.9 ± 2
H2	565.0 ± 4	250.5 ± 9	0.41 ± 0.08	1225.2 ± 15	148.4 ± 2.6
H3	573.50 ± 9	255.0 ± 8.5	0.40 ± 0.11	1236.8 ± 18	151.1 ± 5.8
H4	597.2 ± 6.5	271.5 ± 6	0.38 ± 0.04	1263.5 ± 11	158.9 ± 3
H5	590.1 ± 12	259.2 ± 13	0.39 ± 0.14	1260.6 ± 23	154.2 ± 5.6

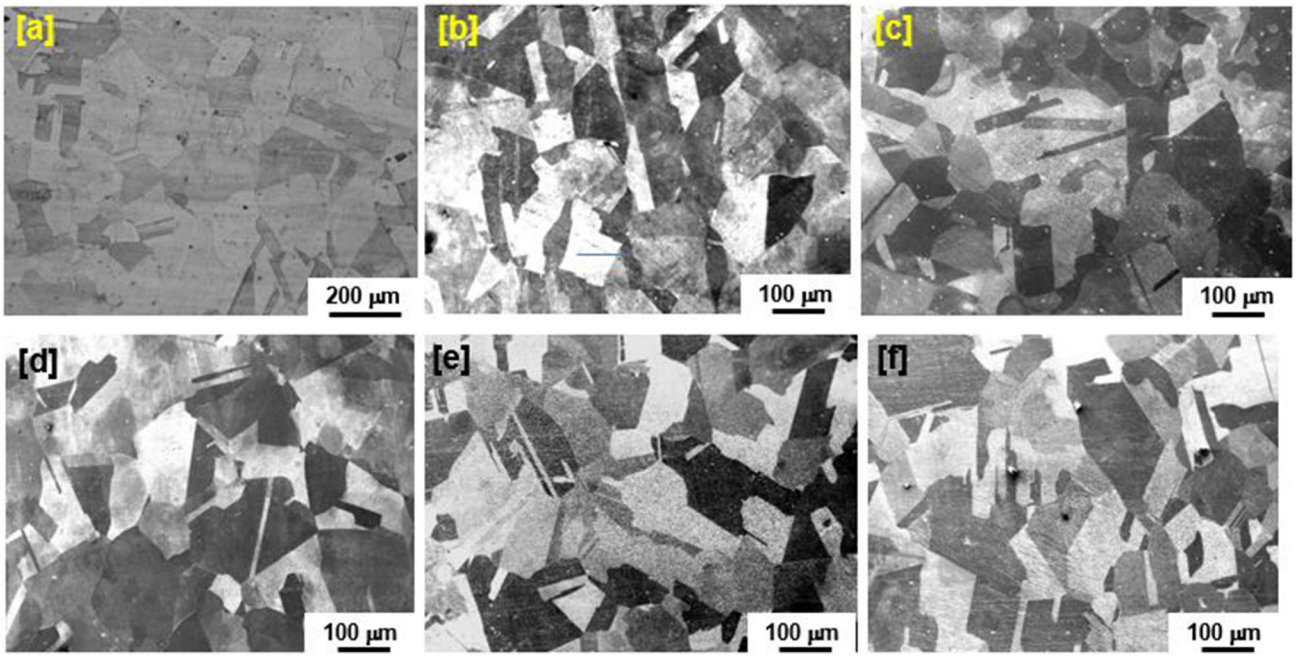

Fig. 6 Optical images of 304 stainless steel (a) as-received, (b) solutionized, (c) solutionized and sensitized at 500 °C (d) solutionized and sensitized at 600 °C, (e) solutionized and sensitized at 700 °C, and (e) solutionized and sensitized at 800 °C

Table 6 Average grain size of solutionized and sensitized 304SS samples

Sample I.D	H	H1	H2	H3	H4	H5
Average grain size (μm)	103 ± 8	173 ± 13	223 ± 17	233 ± 15	281 ± 11	303 ± 9

UTS, YS and fracture toughness of sensitized austenitic stainless steel. In addition, error was calculated for each ANN prediction. A satisfactory agreement has been achieved for mechanical properties, which were obtained using both ball indentation technique and ANN model.

4. Discussion

4.1 Evolution of Microstructure

During solutionization, homogenized single-phase austenite was obtained. It has been illustrated that when 304 austenitic stainless steel is exposed in the temperature range of 450-815 °C over substantial time scale (medium to high temperature sensitization), nearby region of grain boundaries become sensitized (Ref 45). The process includes diffusion of Cr from surrounding matrix and formation of Cr-depleted region around grain boundary (Ref 46). The diffusion of carbon is faster in comparison with the diffusion of chromium. Therefore, the rate controlling step in this process is the diffusion of chromium. Sensitization obeys exponential law of temperature dependence with activation energy ranging from 40 to 70 kcal/mole. This range depends on the nature of as received alloy, which governs the diffusion. High activation energy indicates the diffusion of chromium through the bulk stainless steel. On the other hand, low activation energy corresponds to diffusion of chromium along grain boundaries or dislocation pipes (Ref 47, 48).

Carbide precipitation is influenced by sensitization temperature, duration of thermal exposure, initial matrix grain size and chemical composition. Driving force of precipitation arises due to difference in diffusivity of carbon and chromium in austenite matrix (Ref 49). During isothermal holding, as mentioned above, the preferred location of carbide precipitation becomes grain boundary having high misorientation angle or degree of coincidence. The probable phases within austenitic stainless steel during exposure at 400-900 °C temperature for 10 min to 24 h are ferrite, $M_2(C,N)$, $M_{23}C_6$ and σ (Ref 50). $M_{23}C_6$ appears during short-term aging process. On the contrary, sigma and M_7C_3 can be produced in the long-term thermal exposure. Therefore, the principal second phase after sensitization treatment in the present study becomes Cr carbide ($M_{23}C_6$, where M stands for Cr). The effect of Cr_2N precipitation can be ignored because nitrogen depletion in austenitic matrix becomes dominant at the aging temperature of 750-850 °C for time ranging from 4 h and beyond (Ref 51).

At relatively low sensitization temperature (~ 500 °C), the number of nuclei was trivial due to limited extent of diffusion. This resulted in less number density and small size carbide precipitates, which hindered slip at grain boundary. With the increment in sensitization temperature, diffusion of Cr was accelerated, nucleation time was reduced to achieve critical size and precipitation kinetics was faster with respect to lower temperature. Cr-carbide normally shows low thermal stability; therefore, the number density of precipitates was enhanced along with the increment in average size up to the temperature

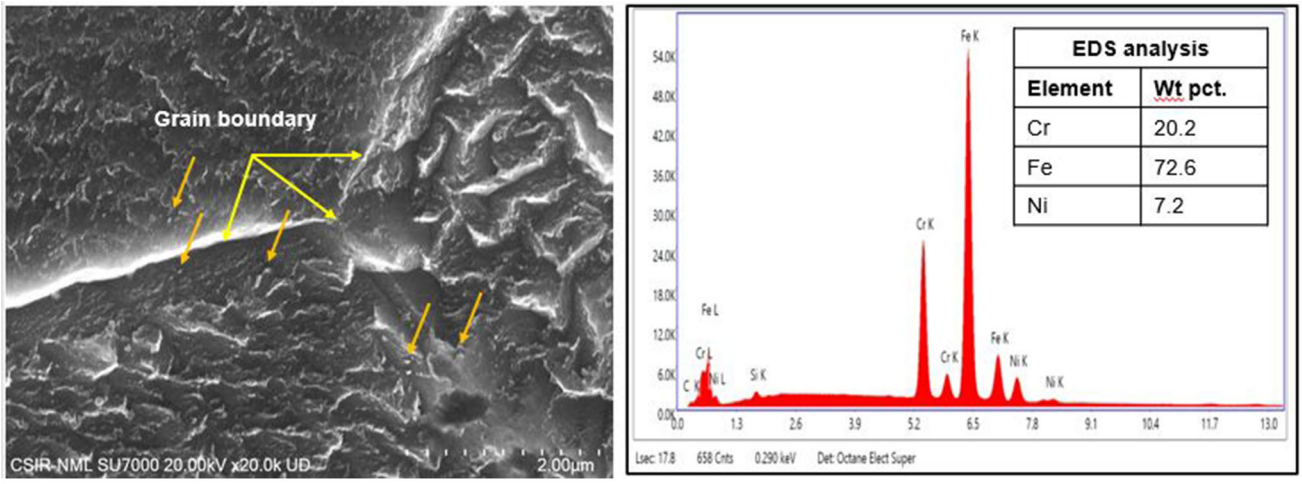

(a)

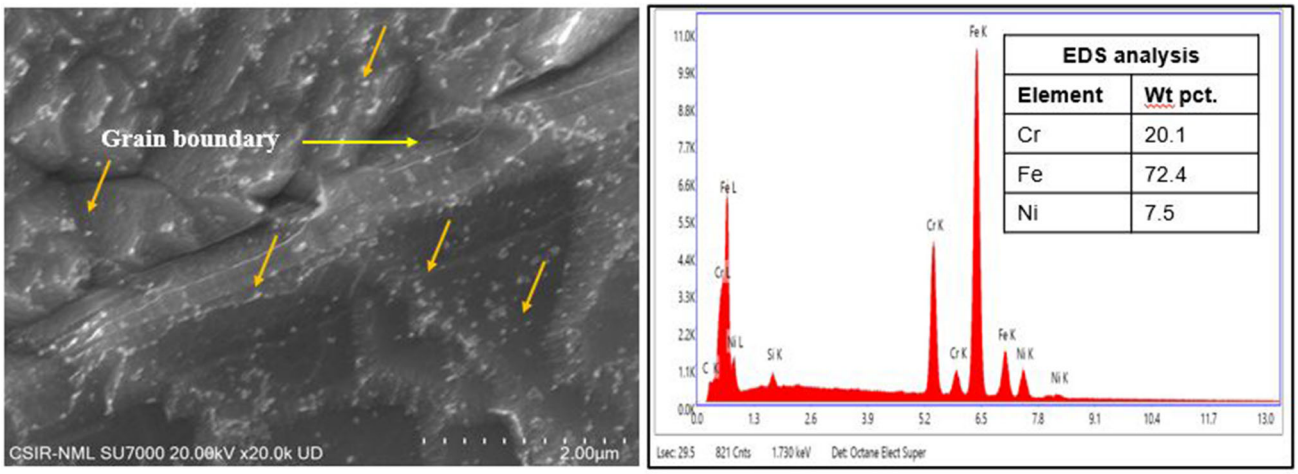

(b)

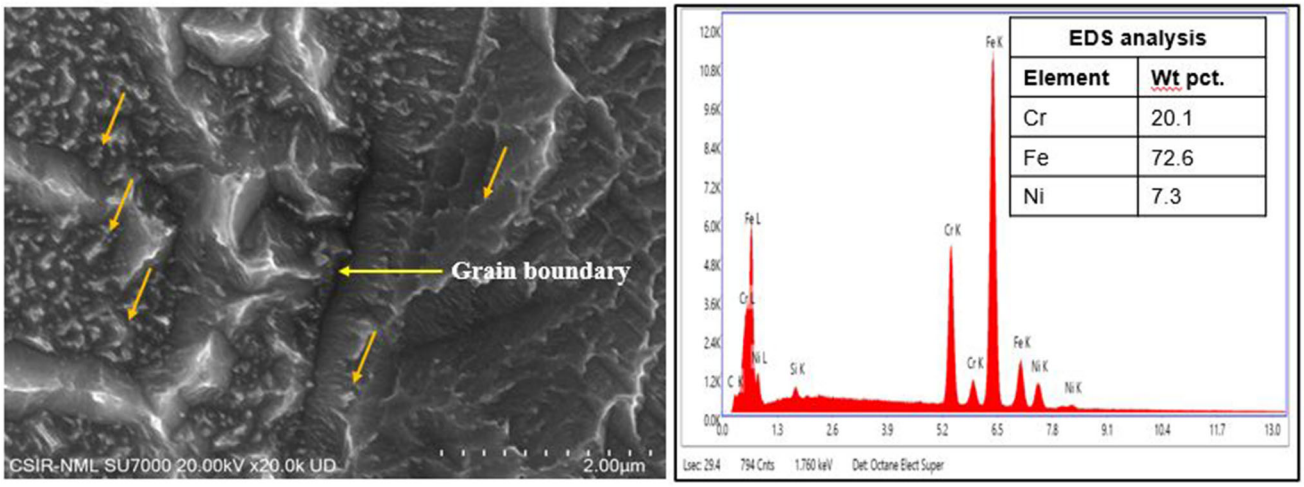

(c)

Fig. 7 (a) SEM micrograph of the sample H2 showing distribution of tiny precipitate (marked by arrow) with semiquantitative elemental analysis of one of the carbides (normalized data). (b) SEM micrograph of the sample H3 showing distribution of precipitates with increased size (marked by arrow) for enhancement in aging temperature along with semiquantitative elemental analysis of one of the carbides (normalized data). (c) SEM micrograph of the sample H5 showing distribution of precipitates with further enhancement in size / coalescence (marked by arrow) at the highest aging temperature along with semiquantitative elemental analysis of one of the carbides (normalized data)

of ~ 700 °C (Ref 52). At the highest sensitizing temperature of ~ 800 °C, the precipitates became interconnected and the average size of individual particle was increased with a diminution in number density (Ref 53, 54).

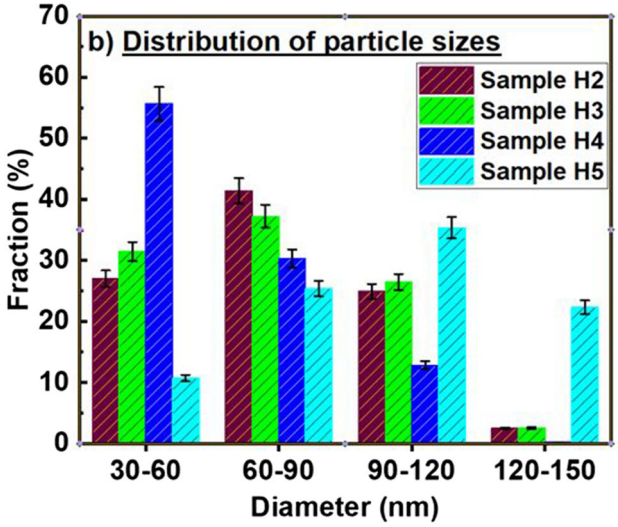

Fig. 8 Distribution pattern of precipitates for different sensitized 304SS specimens

According to Table 6, the matrix grain size of as-received austenitic stainless steel was enhanced many fold at the time of solutionization. During aging at relatively low temperature of 500-600 °C the increment in austenite grain size did not exhibit any quantum jump as previous. At high aging temperature (700-800 °C) once again the increment in matrix grain size was significant and finally attained nearly a slow steady state (Ref 54). At low aging temperature grain boundary pinning was inadequate owing limited quantity of tiny precipitate. Therefore, matrix grain size was increased. With continuous rise in aging temperature, more number of nucleation took place as indicated earlier and increment in the grain size became sluggish. In the same way, high aging temperature (700-800 °C) resulted in coalescence of already formed precipitates and effect of grain boundary pinning was again reduced. The change in number density and average size of precipitate at various thermal conditions have been discussed in the literature for different single-phase and multicomponent systems (Ref 55). The correlation between grain size and precipitation is also available in open domain reports (Ref 54). The present observation becomes at par with earlier findings.

4.2 Mechanical Behavior of Sensitized Specimens

Deformation behavior of any alloy can be explained by the nature of flow curve under stress. While load is applied on material surface through indenter, contact geometry between

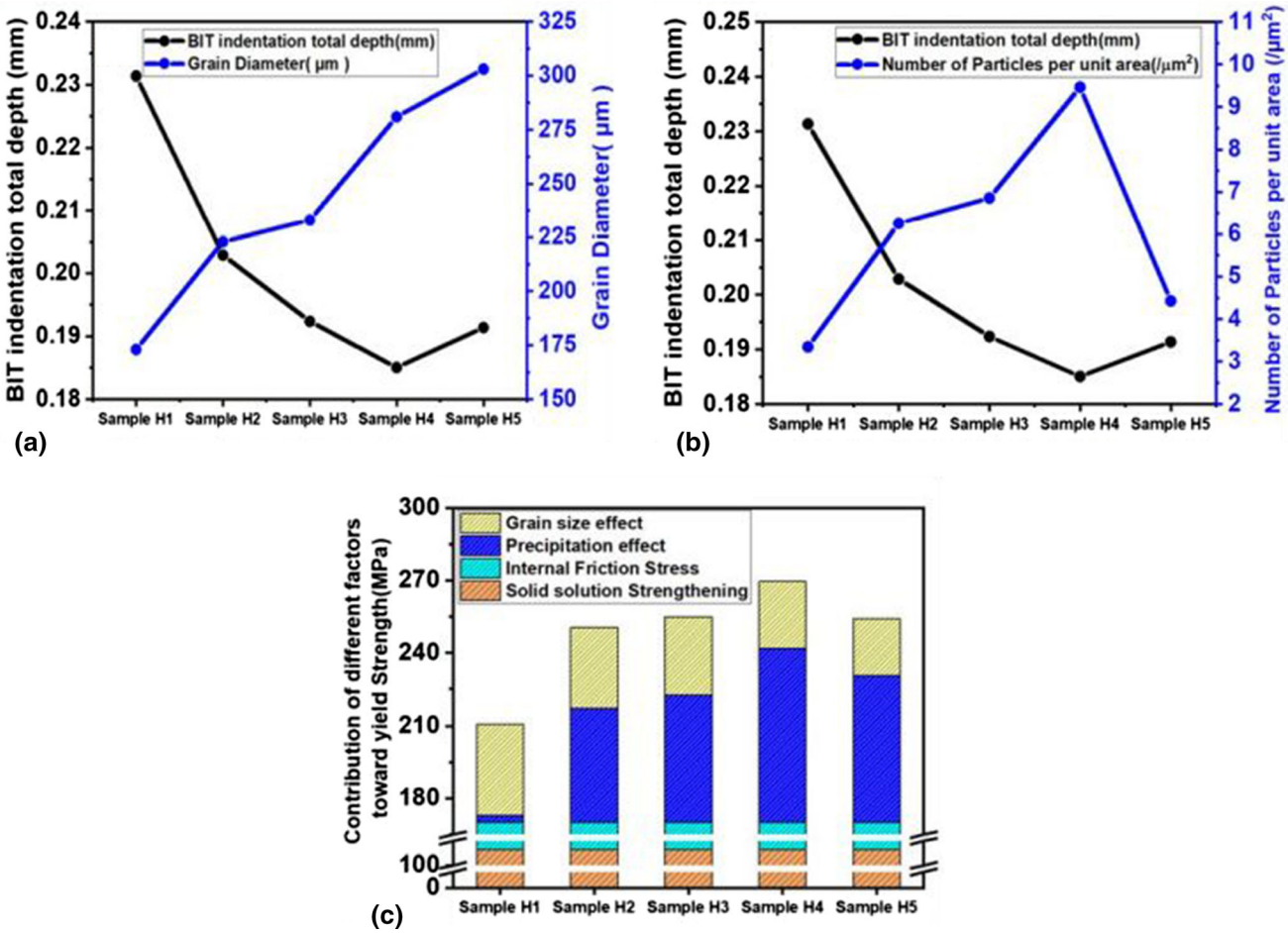

Fig. 9 Microstructural effect on mechanical properties for sensitized 304SS specimens (a) indentation depth-grain size relation, (b) indention depth-area fraction of precipitate relation and (c) contribution of microstructural parameters toward yield strength

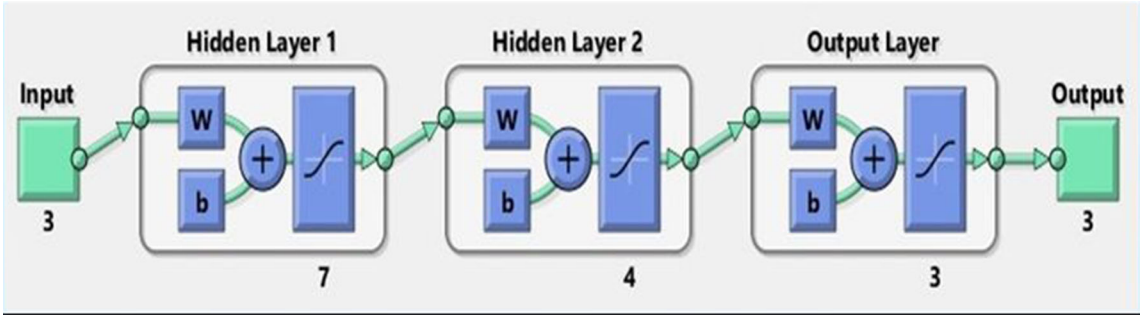

Fig. 10 Schematic of ANN model using MATLAB toolbox

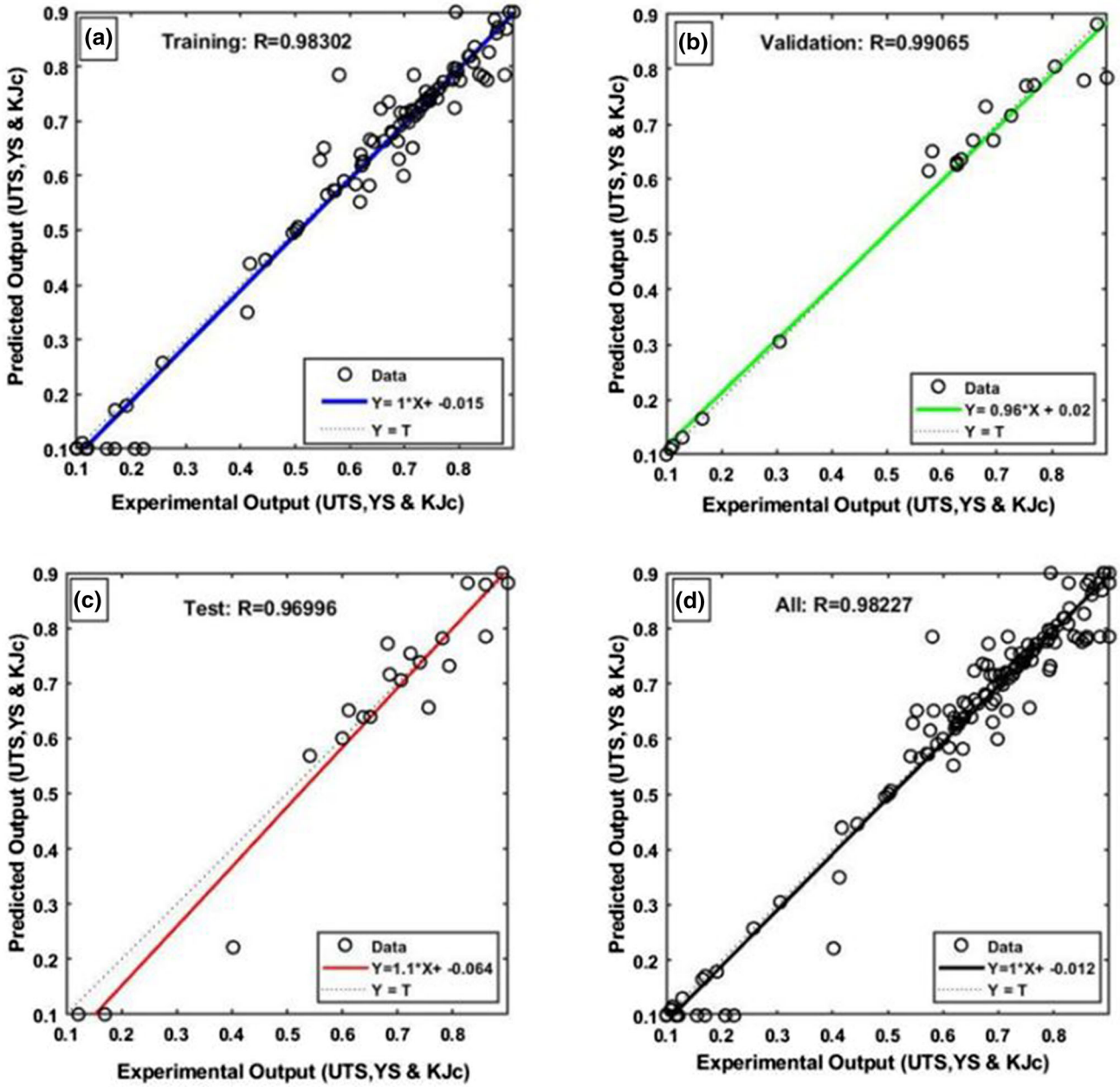

Fig. 11 Correlation of the experimental and predicted output in (a) training, (b) validation, (c) testing and (d) all sets for ANN model

indenter and the alloy changes due to flow of material beneath the indenter. Accuracy of BIT outcome was primarily dependent on applied load and precise measurement of contact area (both total and plastic area) between the indenter and the test specimen. Contact area was determined through the indentation depth using LVDT (Ref 13). Degree of pile-up/sink-in sur-

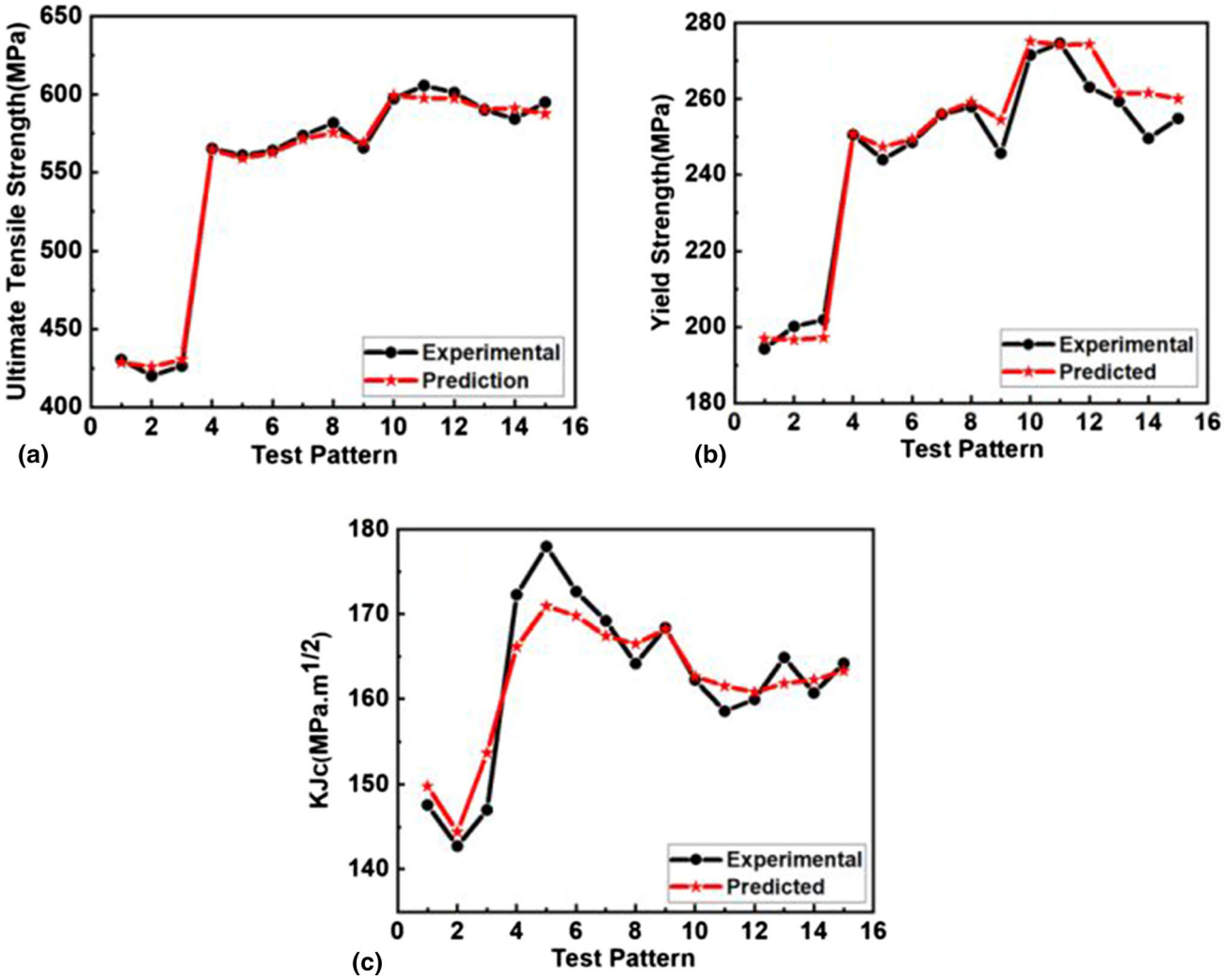

Fig. 12 The plot of experimental and predicted data of sensitized 304SS specimens (a) UTS, (b) YS and (c) fracture toughness

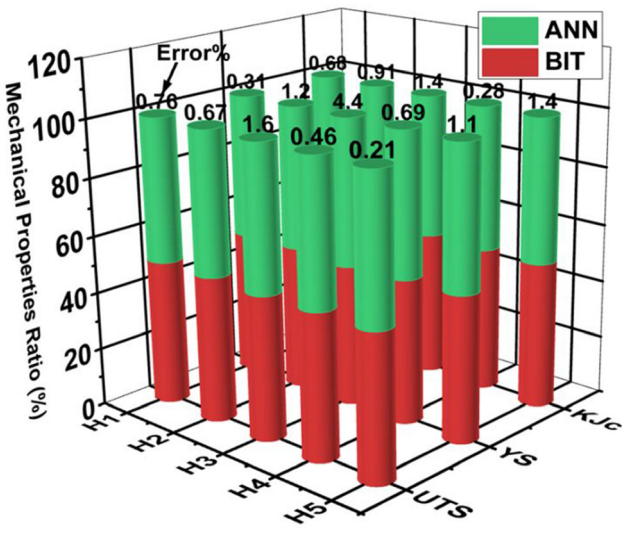

Fig. 13 Comparison of mechanical properties evaluated by ANN and BIT for sensitized 304SS

rounding the indentation was governed by material characteristics and occurred around the indentation profile. Actual contact area might exhibit deviation due to the pile-up/sink-in of materials. Hence, necessary modifications were considered while measuring the indentation depth (Ref 13).

Plastic deformation under compressive load is accompanied by two different contributing parameters apart from microstructural features described above for austenitic stainless steel. One of them is dislocation multiplication between yield and uniform strain. The other one is deformation-induced martensitic transformation, which ensued locally. Both these factors lead to the enhancement of strength and reduce the effect of solid solution strengthening by depleting the dissolved chemical species of austenite matrix. To explore these two aspects were beyond the scope of present investigation.

Flow curves for different sensitized specimens showed distinct differences. Sample H4 presented the maximum increase in strength compare to as-received and other samples. Though the grain size was increased with the increment in sensitization temperature, however, the precipitate contribution was more dominant than that of the former. Significant enhancement in the strength was due to the precipitation as it

Table 7 Experiment data for testing and predicted output from the ANN network

Sample	GS, μm	AF%	Prec. size, nm	UTS, MPa			YS, MPa			KJc, MPa.$\sqrt{m}$		
				M	P	E%	M	P	E%	M	P	E%
H1	173	0.33	82.13	430.4	427.15	0.75	194.26	193.66	0.3	147.59	148.59	0.67
H2	223	0.84	101.01	565.23	561.43	0.67	250.50	247.46	1.21	172.28	170.71	0.9
H3	233	1.03	110.39	573.50	582.87	1.6	255.88	267.05	4.18	169.20	166.9	1.65
H4	281	1.10	100.9	597.25	594.53	0.45	271.52	273.4	0.69	162.25	161.8	0.25
H5	303	0.36	116.4	590.1	588.85	0.21	259.3	256.46	1.095	164.9	162.61	1.38

M = Measured, P = Predicted, E = Error.

hindered the dislocation movement (Ref 56, 57). Therefore, from Sample-H2 to H4, with respect to solutionized specimen, a continuous rise in yield strength, ultimate tensile strength, and fracture toughness were observed (Ref 58). Sample H5 experienced softening during sensitization at 800 °C. Reasons were increment in grain size, appearance of coarse precipitates and decrease in dislocation density owing to thermally activated annihilation (Ref 59, 60). During compressive loading, matrix and precipitate behaved in different ways. The lattice parameter of FCC matrix of austenitic stainless steel was different with respect to Cr-carbide precipitate. This phenomenon generated lattice strain at precipitate-matrix interface (Ref 61). Under stress, dislocations piled up at interface and contributed further to stress concentration. Such excessive stress led to interface decohesion/void formation (Ref 62). It has been also reported that fine-scale dense second phases enhanced the deformation capability of system by hindering void nucleation. On the other hand, increment in size of second phase behaved in opposite way (Ref 63). Considering the fact, at low aging temperature, precipitates were tiny in size; therefore, void formation was limited and plastic deformation was large. With the increment in aging temperature, average size of precipitates was increased. Under stress during indentation early void nucleation was facilitated and deformation became restricted.

Sensitization of 304L stainless steel welded joints at the temperatures of 750-850 °C for 60-120 min reported bulk hardness of 160-178 HV with UTS ~ 538-551 MPa and YS ~ 282-303 MPa (Ref 64). Little higher value of macrohardness and YS with respect to present investigation may be ascribed to smaller duration of heat treatment of the former with respect to latter. In the same context, the tensile strength of AISI 304 SS was found 530, 505 and 460 MPa, after single, double and triple pass welding, respectively. It has been inferred that the tensile strength was principally contributed by chromium carbide precipitation in the sensitized zone (Ref 65). In a different endeavor, 304 stainless were solutionized at 1050 °C, followed by aging at 750 °C for 1-100 h (Ref 66). The YS and UTS were ~ 317 and ~ 670, respectively, for the aged specimens. Little higher value of the tensile properties with respect to present outcome using BIT might be attributed to the minor compositional difference of virgin alloy. In a different attempt, Ti and Mo modified 304 austenitic steel was sensitized in the temperature range of 500-900 °C for an hour (Ref 67). Hardness of the as-received specimen exhibited an increment from ~ 164 to ~ 185 HV after thermal treatment at ~ 700 °C. The change in hardness was marginal beyond 800 °C (~ 186 HV) owing to softening and other counter balancing phenomena.

Fracture toughness of solutionized alloy became substantially higher than as-received austenitic stainless steel owing to single-phase precipitate free structure. With rise in aging temperature, fracture toughness dropped continuously in comparison to solutionized alloy due to the appearance of second phases. At the highest aging temperature of ~ 800 °C, the change in the same was nominal (rather within the scatter band) with respect to (~ 700 °C), due to qualitatively / quantitatively marginal alteration in microstructural features. It is noteworthy that Table 5 also contained 'K,' which refers to 'strength coefficient.' Therefore, the unit of two 'K's' is different and denoted by different suffixes.

It has been experimentally shown that the mechanical properties obtained by conventional tensile test became at par with the data obtained through ball indentation technique for virgin 304 SS. After sensitization, the present study exhibited that ball indentation technique has adequate potential and consistency in evaluating the mechanical properties of the same specimens also, when compared with open domain literature reports. The finding opened up an avenue to eradicate the need of full length mechanical tests for critical components.

4.3 ANN Model for Sensitized Specimens

Experimental values of BIT, the predicted values obtained from ANN using quantified microstructural information, and error percent of tensile parameters are collated in Table 7. The experimental data, which were not used during the learning process, have been selected to examine the accuracy and reliability of ANN model. Out of different primary and secondary microstructural characteristics, the contributory parameters were selected judiciously during the development of ANN model and yielded high R^2 value during addressing yield strength, ultimate tensile strength and fracture toughness for sensitized specimens. Mean square error (MSE) value of predicted output of UTS, YS and fracture toughness was 0.98, 1.52 and 1.01, respectively. Owing to the high value of R^2 and small value of MSE, the developed model exhibited substantial potential and reliability in predicting the mechanical properties of sensitized 304 stainless steel.

5. Summary

Sensitization treatment of 304 stainless steel has been carried out in a temperature range of 500-800 °C for definite time scale. Microstructural parameters like matrix grain size, fraction of precipitates and size range of second phases were estimated. In next step, two different attempts have been made;

in the first one using the quantified microstructural information, an ANN base model was developed to predict the mechanical properties of the alloy. In the second one, mechanical properties of the sensitized alloys were evaluated by ball indentation technique. Finally, a comparison has been drawn between the predicted value and experimental data for same specimen. The major findings of the study are summarized below:

- Increment in sensitization temperature propelled continuous coarsening of matrix grains of 304SS. Precipitate fraction was enhanced with the rise in sensitization temperature, reached maximum at $\sim$ 700 °C and then dropped owing to coalescence of precipitated particles. Nearly similar behavior was observed for the change in average size of Cr-carbide precipitate during sensitization treatment.
- Yield strength, ultimate tensile strength and fracture toughness were estimated using ball indentation technique. All three parameters were increased incessantly with the enhancement in sensitization temperature. The trend was followed up to the temperature of $\sim$ 700 °C and then plummeted during further increment of the same.
- The ANN base model exhibited the same trend in predicting the mechanical properties. The predicted data and experimental results were in perfect match with each other. The impressive reliability of the developed model was attributed to the high R^2 and small MSE values, obtained during the development of same.

BIT proved its reliability for in situ monitoring of mechanical properties of 304SS specimens, exposed in sensitizing environment. At the same time, the mechanical properties can be also predicted by using the developed ANN base model, in which the quantified microstructural data have been considered as input. The present study opened up two-way approaches in foretelling the component efficiency, which was made of 304SS and exposed to sensitization environment.

Acknowledgments

The authors are grateful to The Director, CSIR-National Metallurgical Laboratory for providing the infrastructural support to carry out the investigation and kindly accord permission to publish the work. The authors recognized the support from Mr. Shivmani Singh (M.Tech intern) and Mr. Chandan Dutta (CSIR-SRF) during execution of experiments.

Data Availability

The raw data required to reproduce these findings are not available for download. Similarly, the processed data required to reproduce these findings are also not available.

The justification for non-availability is as follows: The raw/processed data required to reproduce these findings cannot be shared at this time due to legal /ethical reasons. The raw/processed data required to reproduce these findings cannot be shared at this time as the data also forms part of an ongoing study.

References

1. H. Ma, S. Chen, C. Yang and J. Luo, Comparison of the Influence of Nitrate Ions on the Electrochemical Behaviour of Iron and Carbon Steels in Sulphate Solutions, *J. Serbian Chem. Soc.*, 2002, **67**(6), p 425–436.
2. R. Singh, B. Ravikumar, A. Kumar, P.K. Dey and I. Chattoraj, Intergranular Corrosion Behavior of AISI 304 Stainless Steel, *Metall. Mater. Trans. A*, 2003, **34**(November), p 2441–2447.
3. R. Singh, Influence of Cold Rolling on Sensitization and Intergranular Stress Corrosion Cracking of AISI 304 Aged at 500 °CNo Title, *J. Mater. Process. Tech.*, 2008, **206**(1–3), p 286–293.
4. R.Z. Valiev, I.V. Alexandrov, Y.T. Zhu and T.C. Lowe, Paradox of Strength and Ductility in Metals Processed by Severe Plastic Deformation, *J. Mater. Res.*, 2002, **17**(1), p 5–8.
5. J.L. Rempe and D.L. Knudson, High Temperature Thermal Properties for Metals Used in LWR Vessels, *J. Nucl. Mater.*, 2008, **372**(2–3), p 350–357.
6. Y. Kimura, T. Inoue, F. Yin and K. Tsuzaki, Inverse Temperature Dependence of Toughness in an Ultrafine Grain-Structure Steel, *Science (80-.)*, 2008, **320**(5879), p 1057–1060.
7. T. Gladman, Precipitation Hardening in Metals, *Mater. Sci. Technol.*, 1999, **15**(1), p 30–36.
8. K.A. Reddy, Non-destructive Testing, Evaluation of Stainless Steel Materials, *Mater. Today Proc.*, 2017, **4**(8), p 7302–7312.
9. N.M. Tukur, M.S. Dambatta and A. Ahmed, Effect of Heat Treatment Temperature on Mechanical Properties of the AISI 304 Stainless Steel, *Int. J. Innov. Res. Sci. Eng. Technol*, 2014, **3**(2), p 9516–9520.
10. G. Das, M. Das, S. Sinha, K.K. Gupta, S. Chakrabarty and A.K. Ray, Characterization of Cast Stainless Steel Weld Pools by Using Ball Indentation Technique, *Mater. Sci. Eng. A*, 2009, **513–514**(3), p 389–393.
11. G. Das, M. Das, S. Ghosh, P. Dubey and A.K. Ray, Effect of Aging on Mechanical Properties of 6063 Al-Alloy Using Instrumented Ball Indentation Technique, *Mater. Sci. Eng. A*, 2010, **527**(6), p 1590–1594.
12. M. Das, G. Das, M. Ghosh, M. Wegner, V. Rajnikant, S. Ghoshchowdhury and T.K. Pal, Materials Science & Engineering a Microstructures and Mechanical Properties of HPT Processed 6063 Al Alloy, *Mater. Sci. Eng. A*, 2012, **558**, p 525–532. https://doi.org/10.1016/j.msea.2012.08.040
13. M. Das, T.K. Pal and G. Das, Use of Portable Automated Ball Indentation System to Evaluate Mechanical Properties of Steel Pipes, *Trans. Indian Inst. Met.*, 2012, **65**(2), p 197–203.
14. M. Das, T.K. Pal and G. Das, Effect of Aging and Cryo Rolling on Microstructural Characterization and Mechanical Properties of Precipitation Hardenable 6063Al Alloy, *Mater. Sci. Eng. A*, 2012, **552**, p 31–35. https://doi.org/10.1016/j.msea.2012.04.104
15. K. Sharma, H.K. Khandelwal, V. Bhasin and R. Chhibber, Application of Ball Indentation Technique for Mechanical Properties Estimation of Bi-Metallic Weld, *Adv. Mater. Res.*, 2012, **585**, p 342–346.
16. D. Barbadikar, A. Ballel, D. Peshwe, T. Sakthivel, and M Methew, Application of the Ball Indentation Technique to Study the Tensile Properties across the P92 Steel Weld Joint, Adv. Mater. Struct. Mech. Eng. - Proc. Int. Conf. Adv. Mater. Struct. Mech. Eng., (2016), 11–16
17. M.K. Samal, A. Syed, R.N. Khatri and J. Chattopadhyay, Study of Plastically Deformed Region Underneath the Ball in Indentation Tests and Evaluation of Mechanical Properties of Materials Through Finite Element Simulation and a Hybrid Algorithm, *J Mech. Engg. Sci.*, 2021, **235**(1), p 108–121.
18. H. Xue, J. He, J. Zhang and Y. Xue, Approach for Obtaining Material Mechanical Properties in Local Region of Structure Based on Accurate Analysis of Micro-Indentation Test, *Chinese J. Mech. Eng.*, 2021, **34**, p 130–142. https://doi.org/10.1186/s10033-021-00644-6)
19. K. Rahmani, A. Nouri, G. Wheatley, H. Malekmohammadi, H. Bakhtiari and V. Yazdi, Determination of Tensile Behavior of Hot-Pressed Mg-TiO_2 and Mg-ZrO_2 Nanocomposites Using Indentation Test and a Holistic Inverse Modelling Technique, *J Mater. Sci. Technol.*, 2021, **14**(2107), p 2114.
20. T.T. Chen, I. Watanabe, D. Liu and K. Goto, Data-Driven Estimation of Plastic Properties of Alloys Using Neighbouring Indentation Test, *Sci. Technol. Adv. Mater. Methods*, 2021, **1**(1), p 143–151.
21. C.S. Maunoury, A. Albayada, O. Bartier, L. Weiss, G. Mauvoisin, X. Hernot and P. Laheurte, On the use of Instrumented Indentation to Characterize the Mechanical Properties of Functionally Graded Binary

Alloys Manufactured by Additive Manufacturing, *Mate. Today Comm.*, 2020, **25**, p 101451. https://doi.org/10.1016/j.mtcomm.2020.101451)
22. J. Lee, K. Lee, S. Lee, O.M. Kwon, W.K. Kang, J. II Lim, H.K. Lee, S.M. Kim and D. Kwon, Application of Macro-Instrumented Indentation Test for Superficial Residual Stress and Mechanical Properties Measurement for HY Steel Welded T-Joints, *Materials*, 2021, **14**, p 2061–2074. https://doi.org/10.3390/ma14082061
23. D. R. Barbadikar, A. R. Ballal, D. R. Peshwe, T. Sakthivel, M.D. Mathew, Application of the Ball Indentation Technique to Study the Tensile Properties Across the P92 Steel Weld Joint, in *Advanced Materials, Structures and Mechanical Engineering*, Kaloop (Ed.), (2016), p.11–15
24. K. Sharma, H.K. Khandelwal, V. Bhasin and R. Chhibber, Application of Ball Indentation Technique for Mechanical Properties Estimation of bi-Metallic Weld, *Adv. Mater. Res.*, 2012, **585**, p 342–346.
25. M. S. Mhatre, D. Siddiqui, M. Dongre, P. Thakur, A Review Paper on Artificial Neural Networks: A Prediction Technique, Int. J. Sci. Eng. Res., **6**(12), 161–163 (2015), http://www.ijser.org
26. S. Agatonovic-Kustrin and R. Beresford, Basic Concepts of Artificial Neural Network (ANN) Modeling and Its Application in Pharmaceutical Research, *J. Pharm. Biomed. Anal.*, 2000, **22**(5), p 717–727.
27. S. Pyo, J. Lee, M. Cha and H. Jang, Predictability of Machine Learning Techniques to Forecast the Trends of Market Index Prices: Hypothesis Testing for the Korean Stock Markets, *PLoS ONE*, 2017, **12**(11), p 1–17.
28. D. Merayo, A. Rodriguez-Prieto and A.M. Camacho, Prediction of Physical and Mechanical Properties for Metallic Materials Selection Using Big Data and Artificial Neural Networks, *IEEE Access*, 2020, **8**, p 13444–13456.
29. D.M. Dimiduk, E.A. Holm and S.R. Niezgoda, Perspectives on the Impact of Machine Learning, Deep Learning, and Artificial Intelligence on Materials, Processes, and Structures Engineering, *Integr. Mater. Manuf. Innov.*, 2018, **7**(3), p 157–172.
30. J. Ling, E. Antono, S. Bajaj, S. Paradiso, M. Hutchinson, B. Meredig, B.M. Gibbons, Machine Learning for Alloy Composition and Process Optimization," in *Proceedings of the ASME Turbo Expo*, American Society of Mechanical Engineers (ASME), (2018)
31. S. J. T. Thankachan, K. S. Prakash, C. D. Pleases, D. Rammasamy, B. Prabakaran, Machine Learning for Degraded Mechanical Properties of Metallic Materials Due to the Presence of Hydrogen, Int. J. Hydrogen Energy, (2017)
32. G. Partheepan, D.K. Sehgal and R.K. Pandey, Quasi-Non-Destructive Evaluation of Yield Strength Using Neural Networks, *Adv. Artif. Neural Syst.*, 2011, **2011**, p 1–8.
33. S. Malinov, W. Sha and J.J. McKeown, Modelling the Correlation Between Processing Parameters and Properties in Titanium Alloys Using Artificial Neural Network, *Comput. Mater. Sci.*, 2001, **21**(3), p 375–394.
34. J.M.C. McElfresh, C. Roberts, S. He and S. Prikhodko, Using Machine-Learning to Understand Complex Microstructural Effects on the Mechanical Behavior of Ti-6Al-4V Alloys, *Comput. Mater. Sci.*, 2022, **208**, p 111267.
35. S. Kolli, T. Ohligschlager, D. Porter, Continuous Cooling Sensitization and its Evaluation in Austenitic Stainless Steel EN 1.4310, ESSC & Duplex 2017 Proceedings
36. K.N. Jang, T.K. Kim and K.T. Kim, The Effect of Cooling Rates on Carbide Precipitate and Microstructure of 9CR-1MO Oxide Dispersion Strengthened(ODS) Steel, *Nuclear Engg. and Technol.*, 2019, **51**, p 249–256.
37. T.H. Chen, K.L. Weng and J.R. Yang, The Effect of High-Temperature Exposure on the Microstructural Stability and Toughness Property in a 2205 Duplex Stainless Steel, *Mater. Sci. Eng. A*, 2002, **338**(1–2), p 259–270.
38. M.D. Mathew, J. Ganesh Kumar, V. Ganesan and K. Laha, Ball Indentation Studies on the Effect of Nitrogen on the Tensile Properties of 316LN SS, *High Temp. Mater. Process.*, 2015, **34**(8), p 827–832.
39. A. Eres-Castellanos, I. Toda-Caraballo, A. Latz, F.G. Caballero and C. Garcia-Mateo, An Integrated-Model for Austenite Yield Strength Considering the Influence of Temperature and Strain Rate in Lean Steels, *Mater. Des.*, 2020, **188**, p 108435. https://doi.org/10.1016/j.matdes.2019.108435
40. M. Farooq, Doctoral thesis on 'Strengthening and degradation mechanisms in austenitic stainless steels at elevated temperature', at Dept. of Mater. Sci. and Engg. Royal Inst. of Technol. (KTH) SE-100 44 Stockholm, Sweden, (2013), pp. 5–10, https://www.diva-portal.org/smash/get/diva2:621120/FULLTEXT01.pdf
41. C. F. Willis, A Study of Chromium Carbide Precipitationat Interphase Boundaries in Stainless Steel Welds, A Report of Mater. and Chem. Sci. Div., National Center for Electron Microscopy, Lawrence Berkeley Laboratory University of California, Berkeley, 1990), pp. 2–15, https://www.osti.gov/servlets/purl/6552861
42. M.W. Mahoney and N.E. Paton, The Effect of Carbide Precipitaionon Fatigue Crack Propagationin Type 316 Stainless Steel, *Nuclear Technol.*, 2017, **23**, p 53–62. https://doi.org/10.13182/NT74-A31433
43. S. Kolli, V. Javaheri, J. Komi and D. Porter, On the Role of Grain Sizeand Carbon Content on Thesensitization nad Desensitization Behaviour of 301 Austenitic Stainless Steel, *Metals*, 2019, **9**, p 1–15.
44. Y.J. Wang, R.B. Song and R.F. Song, Phase Transformation and Carbide Precipitation of Functional Gradient Semi-Solid 9Cr18 Steel, *Acta Met. Sinicia*, 2018, **31**(8), p 823–830.
45. A. Bahrami and P. Taheri, A Study on the Failure of AISI 304 Stainless Steel, *Metals (Basel)*, 2019, **9**, p 969.
46. T. Jia, R. Ni, H. Wang, J. Shen, Z. Wang, Investigation on the Formation of Cr-rich Precipitates at the Interphase Boundary in type 430 Stainless Steel Based on Austenite-Ferrite Transformation Kinetics, Metals (Basel), **9**(10), (2019)
47. M. J. Fox, R. D. Mccright, An Overview of Low Tempearture Sensitization, (1983), (December)
48. G. Choudhuri, A.K. Sinha, V. Kain, K.R. Gurumurthy and B.K. Shah, Low Temperature Sensitization of Austenitic Stainless Steel, *Trans. Indian Inst. Met.*, 2003, **56**(1), p 79–84.
49. S. Kolli, *Sensitization in Austenitic Stainless Steels: Quantitative Prediction Considering Multicomponent Thermodynamic and Mass Balance Effects*, (2020)
50. F. Qin, Y. Li, W. He, X. Zhao and H. Chen, Aging Precipitation Behavior and its Influence on Mechanical Properties of Mn18Cr18N Austenitic Stainless Steel, *Met. Mater. Int.*, 2017, **23**(6), p 1087–1096.
51. H. Kong and C. Liu, A Review on Nano-Scale Precipitation in Steels, *Technologies*, 2018, **6**(1), p 36.
52. M. Vach, T. Kuníková, M. Dománková, P. Ševc, Ľ Čaplovič, P. Gogola and J. Janovec, Evolution of Secondary Phases in Austenitic Stainless Steels during Long-Term Exposures at 600, 650 and 800 °C, *Mater. Charact.*, 2008, **59**(12), p 1792–1798.
53. S.H. Lee, J.Y. Choi and W.J. Nam, Hardening Behavior of a 304 Stainless Steel Containing Deformation-Induced Martensite during Static Strain Aging, *Mater. Trans.*, 2009, **50**(4), p 926–929.
54. D.M. Xu, G.Q. Li, X.L. Wan, R.D.K. Misra, X.G. Zhang, G. Xu and K.M. Wu, The Effect of Annealing on the Microstructural Evolution and Mechanical Properties in Phase Reversed 316LN Austenitic Stainless Steel, *Mater. Sci. Eng. A*, 2018, **720**, p 36–48.
55. N. Safara, A. Golpayegani, G. Engberg and J. Agren, Study of the Mean Size and Fraction of the Secondphase Particles in a 13% Chromium Steel at High Temperature, *Phil. Mag.*, 2020, **100**(2), p 217–233.
56. H. Bhadeshia and R. Honeycombe, "Steels: Microstructure and Properties: Microstructure and Properties," 2011
57. S. Muraishi, Internal Stress and Dislocation Interaction of Plate Shaped Misfitting Precipitates in Al alloy, *Materials (basel)*, 2021, **14**(19), p 5811–5821. https://doi.org/10.3390/ma14195811
58. C.R. Hutchinson, J.F. Nie and S. Gorsse, Modeling the Precipitation Processes and Strengthening Mechanisms in a Mg-Al-(Zn) AZ91 Alloy, *Metall. Mater. Trans. A Phys. Metall. Mater. Sci.*, 2005, **36**(8), p 2093–2105.
59. M.V. Kumar, V. Balasubramanian and A. Gourav Rao, Hot Tensile Properties and Strain Hardening Behaviour of Super 304HCu Stainless Steel, *J. Mater. Res. Technol.*, 2017, **6**(2), p 116–122. https://doi.org/10.1016/j.jmrt.2016.05.004
60. Z.F.Z. Du, Z. Deng, A. Xiao, X. Cui and H. Yu, Effect of the Aging Process on the Micro-Structure & Properties of 7075 Aluminum Alloy Using Electromagnetic Bulging, *J. Manuf. Process.*, 2021, **70**, p 15–23.
61. A. Elzas, Nano-scale Failure in Steel Interface Decohesion at Iron/Precipitate Interfaces, Ph.D dissertation submitted to Delft University of Technology, (2019), pp. 7–9, https://doi.org/10.4233/uuid:f72f61f4-4508-4552-85b8-d89abbbee90e
62. E. Barbé, C.C. Fu and M. Sauzay, Fracture of Coherent Interfaces Between an FCC Metal Matrix and the $Cr_{23}C_6$ Carbide Precipitate from First Principles, *Phys. Rev. Mater.*, 2018, **2**, p 023605.

63. Y. Tang, C. Xie, J. Chen and X. Wang, Atomistic Insights into the Competition Between Damage and Dynamic Recrystallization Stimulated by the Precipitate $Mg_{17}Al_{12}$ in Magnesium Alloys, *Metals*, 2022, **12**, p 632–644. https://doi.org/10.3390/met12040633
64. V. Kumar, P. Joshi, S. Dhakad, H. Shekhar, S. Singh and S. Kumar, Analysis of the Effect of Sensitization on Austenitic Stainless Steel 304L Welded by GTAW Process, *HCTL Open Int J. Technol. Innov. Res.*, 2015, **14**(April), p 1–121.
65. R.V. Taiwade, A.P. Patil, R.D. Ghugal, S.J. Patre and R.K. Dayal, Effect of Welding Passes on Heat Affected Zone and Tensile Properties of AISI 304 Stainless Steel and Chrome-Manganese Austenitic Stainless Steel, *ISIJ Int.*, 2013, **53**(1), p 102–109.
66. S. Ghosh, V. Kain, A. Ray, H. Roy, S. Sivaprasad, S. Tarafder and K.K. Ray, Deterioration in Fracture Toughness of 304LN Austenitic Stainless Steel Due to Sensitization, *Metall. Mater. Trans. A Phys. Metall. Mater. Sci.*, 2009, **40**(12), p 2938–2949.
67. S.F. Hasan and S.I.J. Alrubaiey, Effect of Sensitization on Microhardness and Corrosion Resistance of Austenitic Stainless Steel, *Int. J. Comput. Appl. Sci.*, 2017, **2**(2), p 112–115.